



## Article

# Enhanced Oxygen Mass Transfer in Mixing Bioreactor Using Silica Microparticles

Matheus M. Pereira <sup>1</sup>, Ivus Lorenzo Oliveira Matos <sup>2</sup>, Filipe Moreira Mascarenhas Cordeiro <sup>3</sup>, Ana Cristina Morais da Silva <sup>3</sup>, Eliane Bezerra Cavalcanti <sup>2,4</sup> and Álvaro Silva Lima <sup>3,\*</sup>

<sup>1</sup> CERES, Department of Chemical Engineering, University of Coimbra, Rua Sílvio Lima, Pólo II—Pinhal de Marrocos, 3030-790 Coimbra, Portugal; matheus@eq.uc.pt

<sup>2</sup> Post-Graduated Program on Process Engineering, Tiradentes University, Avenida Murilo Dantas, 300, Farolândia, Aracaju 49032-490, SE, Brazil; ivus.lorenzo@hotmail.com (I.L.O.M.); ebcavalcanti@gmail.com (E.B.C.)

<sup>3</sup> Post-Graduated Program on Chemical Engineering, Federal University of Bahia, Rua Aristides Novis, Federação, Salvador 40210-910, BA, Brazil; filipemoreira1@hotmail.com (F.M.M.C.); acristinasilva@ufba.br (A.C.M.d.S.)

<sup>4</sup> Instituto de Tecnologia e Pesquisa, Avenida Murilo Dantas, 300, Prédio do ITP Farolândia, Aracaju 49032-490, SE, Brazil

\* Correspondence: aslima2001@yahoo.com.br

**Abstract:** This work aimed to improve the oxygen transfer mass coefficient ( $k_L a$ ) in mixing reactors, first evaluating the effect of agitation and aeration and then evaluating the influence of the size and concentration of silica microparticles. Silicon dioxide synthesized via the sol-gel technique, commercial sand, and beach sand were characterized by particle size distribution, scanning electron microscopy, XRD, EDS, FTIR, TG/DTA, and BET. The particles presented average values of approximately 9.2, 76.9, 165.1, and 364.4  $\mu\text{m}$ , with irregular surfaces and different roughness. Silica sol-gel is amorphous while beach and commercial sand have a crystalline structure consisting of silicon, oxygen, and carbon residues. Silica sol-gel presents a higher loss of mass and surface area than other silica microparticles, with a shallow mass loss and a smaller surface. Increasing aeration and agitation improves the  $k_L a$ , as well as adding silica microparticles. The best  $k_L a$  was found using silica microparticles with approximately 75  $\mu\text{m}$  concentrations of 1.0  $\text{g L}^{-1}$  (silica sol-gel) and 2.0  $\text{g L}^{-1}$  (commercial and treated beach sand). All silica microparticles used in this work improve mass transfer performance in mixing bioreactors.

**Keywords:** oxygen mass transfer coefficient; aeration; agitation; silica microparticles



**Citation:** Pereira, M.M.; Matos, I.L.O.; Cordeiro, F.M.M.; Silva, A.C.M.d.; Cavalcanti, E.B.; Lima, Á.S. Enhanced Oxygen Mass Transfer in Mixing Bioreactor Using Silica Microparticles. *Fermentation* **2024**, *10*, 255. <https://doi.org/10.3390/fermentation10050255>

Academic Editor: Thaddeus Ezeji

Received: 8 April 2024

Revised: 9 May 2024

Accepted: 11 May 2024

Published: 14 May 2024



**Copyright:** © 2024 by the authors. Licensee MDPI, Basel, Switzerland. This article is an open access article distributed under the terms and conditions of the Creative Commons Attribution (CC BY) license (<https://creativecommons.org/licenses/by/4.0/>).

## 1. Introduction

In microbial growth, oxygen functions as the final electron acceptor [1], and its availability in the environment affects and limits the conduction of the aerobic bioprocess [2]. Microbial metabolism decreases in oxygen-limiting conditions [3], reducing the yield of secondary metabolites [4].

The oxygen supply to the culture medium usually needs to be more efficient due to the low solubility of oxygen in aqueous solutions [5], which is influenced by the concentration of solutes in the medium and temperature [6,7]. Nevertheless, the transfer of oxygen cannot be significantly improved by manipulating the temperature since the rate of transfer of  $\text{O}_2$  is slightly altered in the range of interest of the majority of bioprocesses (25 and 35 °C). Another factor to consider is that the presence of salts decreases the oxygen solubility and, consequently, the mass transfer since an increase in solubility of 0–8% results in dissolved oxygen being reduced from 200.4 to 192.3  $\text{mmol O}_2 \text{ L}^{-1}$  [8].

In studies on the oxygen transfer in multiphase reactors, an alternative to enhance the oxygenation is the use of a second liquid phase rich in dissolving oxygen, such as

perfluorodecalin [9,10]; the addition of solid particles to promote the shearing of oxygen bubbles, thus making the oxygen more soluble in the medium [11,12]; and studies using nanofluids [13,14] and ionic liquids [15] as carriers of oxygen.

According to Littlejohns and Daugulis [11], the use of solid particles in bioreactors to improve mass transfer, and particularly the measurement of the volumetric mass transfer coefficient ( $k_La$ ), is related to different phenomena: (i) adsorbent solid particles enter the boundary layer, adsorb oxygen, and then dissolve it in the bulk phase; (ii) there is an increase in turbulence at the solid–liquid interface, causing the mixing of the boundary layer and consequently an increase in the  $k_La$ ; (iii) solid particles at the solid–liquid interface cause the inhibition of bubble coalescence and increase in the interfacial area.

Several authors have studied the use of particle solids to improve the  $k_La$ . According to Labbeiki et al. [16], nanomaterials positively affect the biochemistry of the fermentation process. Magnetite nanoparticles (0.02 *v/v*) increased, by 1.89 times, the  $k_La$  and, by 2.25 times, the erythromycin production. Fatollahi et al. [17] observed that the positive effect in biomass concentration and ectoine production was reached using the operational condition with the best oxygen mass transfer and multiwalled carbon nanotube or iron oxide nanoparticle. Moreover, large vegetable solid particles such as sugarcane bagasse in an air-lift bioreactor led to the highest  $k_La$  values (0.049  $s^{-1}$ ) and a particle concentration of 10  $g L^{-1}$  [18].

Silicon oxide ( $SiO_2$ ) particles also enhanced the  $k_La$  in previous studies. Ojima et al. (2015) [19] studied the effect of particle diameter on the coalescence of bubbles in a slurry bubble column and found that the time required for bubble coalescence increases with a decrease in particle size from 150 to 60  $\mu m$ . Sasaki et al. [20] reported that increasing the concentration of silica microparticles (100  $\mu m$ ) influences the hold-up of a bubble column until reaching the equilibrium state at a rate of 0.40.

Zhang et al. [21] observed that  $SiO_2$  microparticles such as powdered activated carbon,  $Al_2O_3$ , and  $MnO_2$  particles facilitate oxygen transfer in a bioreactor. Still, this depends on the process's flow regime, which reduces the liquid layer of nearby air bubbles and increases the  $k_La$ . However, using solid particles in the fermenter can lead to the hydrodynamic shearing of the biomass, impacting the morphology and viability of bacterial biomass [22] and even filamentous fungi more susceptible to shearing [23]. In this sense, the use of particles can be administered by limiting the aeration and agitation conditions of the medium.

This work aimed to expand the study of the effect of inserting silica microparticles (sol-gel silica, commercial sand, and beach sand treated with acid–base abrasion), using a low agitation speed to avoid the shear of biomass, in a bioreactor in terms of improving  $k_La$ , evaluating the possibility of using natural microparticles in the aeration process, which had not yet been observed in the literature.

## 2. Materials and Methods

### 2.1. Silica

The sol-gel silica particles were prepared using the methodology developed by Soares et al. [24,25]. The solution formed by tetraethyl orthosilicate (TEOS) was dissolved in absolute ethanol under an inert atmosphere of nitrogen, in which we added hydrochloric acid in ethanol (35% dissolved in ultrapure water solution (pre-hydrolyzing). After slowly adding the solution pre-hydrolyzing, the temperature was maintained at 35 °C, and the mixture was left under stirring for 90 min. It was added to an ammonium hydroxide solution dissolved in ethanol (solution hydrolyzing), and then the mixture was kept at rest for 24 h to allow complete polycondensation. After this period, the material was opened, dried, and homogenized.

The commercial sand (silicon dioxide washed and calcined with acid) used was obtained from Sigma-Aldrich, with the formation of particle size of 0.1 to 0.3 mm (min. 96%).

A sample of beach sand (1 kg) was collected in the beach city of Aracaju-SE, Brazil and subjected to an abrasive acid–base treatment process. Initially, the resuspended sample

of 100 g of sand was left in HCl (3 M) for 24 h, then washed with water and resuspended in NaOH (3 M) for 24 h to neutralize, followed by washing in running water and drying. After this pretreatment, a new abrasive was made using HCl (6 M) and NaOH (10 M), followed by washing with distilled water until the pH of the washing water became neutral. The process was finalized by drying at 105 °C. The sand thus treated was stored in airtight containers in cool, dry places.

#### Silica Characterization

The synthesized silica particles, treated beach sand, and silicon dioxide were analyzed using light microscopy to determine the size and the particle size distribution. An aliquot of particles obtained through the methodology of the quarters was dispersed on glass slides, and about 30 photomicrographs were obtained using an inverted microscope (Zeiss Axiovert 40 MAT Model, Oberkochen, Germany). The particle size was determined by measuring about 2000 particles in the photomicrographs obtained with the aid of the software REL.4.7 Axion Vision. An overall average was used to determine size distribution and average particle size brought by the graph versus frequency.

The silica microparticle morphology was analyzed using Scanning Electronic Microscopy—SEM (Hitachi SU-70, Tokyo, Japan). Elemental analysis was performed using an energy-dispersive X-ray—EDS probe attached to the same SEM described above.

The X-ray diffraction was performed on Phillips X'pert Diffractometer equipment (Amsterdam, The Netherlands). The diffracted intensity of Cu K $\alpha$  radiation ( $\lambda = 0.1541$  nm, 40 Kv, and 50 mA) was determined in a  $2\theta$  range between 10 and 45°.

Particles were also submitted to the Fourier transform infrared-FTIR analysis (Perkin Elmer Spectrum Bx, Waltham, MA, USA), with Attenuated Total Reflectance (ATR) at 4 cm<sup>-1</sup> resolution and eight scans. The spectra were obtained in the wavelength range from 400 to 4000 cm<sup>-1</sup>.

The weight loss of the silica microparticle sample upon heating was determined in a thermogravimetric analysis (TGA) apparatus (TGA-50 Shimadzu—Thermogravimetric Analyzer, Kyoto, Japan) over the range 25–600 °C, with a heating rate of 20 °C min<sup>-1</sup>, using air as the purge gas. Differential scanning calorimetry data were processed in a Perkin Elmer DSC-50 differential scanning calorimeter (Shelton, CT, USA).

Textural characteristics of the outgassed samples were obtained from nitrogen physisorption using a Quantachrome instrument, Nova 2000 series (Graz, Austria). The specific surface area meant that cylindrical pore diameters and adsorption pore volume were determined. Before the measurements, the samples were degassed to 50 mmHg at 300 °C during 3 h. Based on the nitrogen adsorption data, the BET specific surface area (m<sup>2</sup>g<sup>-1</sup>) was calculated using the standard Brunauer, Emmett, and Teller methods. The pore size (Å) and pore volume (cm<sup>3</sup>g<sup>-1</sup>) were calculated by applying the Barrett–Joyner–Halenda (BJH) method to the desorption branches of the isotherms. The IUPAC classification of pores and isotherms was used in this study.

#### 2.2. Determination of the Volumetric Mass Trans Coefficient ( $k_L a$ )

The volumetric coefficient of oxygen transfer was determined using the dynamic gassing out method. Experimental procedures were carried out in a cylindrical bioreactor of 4.5 L with a working volume of 3.0 L (Tecnal—Piracicaba, Brazil)—the glass vessel present dimension described in Figure 1. The impeller types were the Rushton turbine (bottom) and the Smith turbine (top). The system was agitated at speeds between 50 and 200 rpm and aeration rate between 0.5 and 6.0 L min<sup>-1</sup>. The experiments were performed at atmospheric pressure, and the temperature was controlled at 25 °C, causing a water bath that circulates water through the plate on the bottom of the bioreactor; the pH value was 7.0. Dissolved oxygen was monitored by a polarographic oxygen electrode (Mettler Toledo—O<sub>2</sub> Sensor, Greifensee, Switzerland) connected to a data acquisition meter.

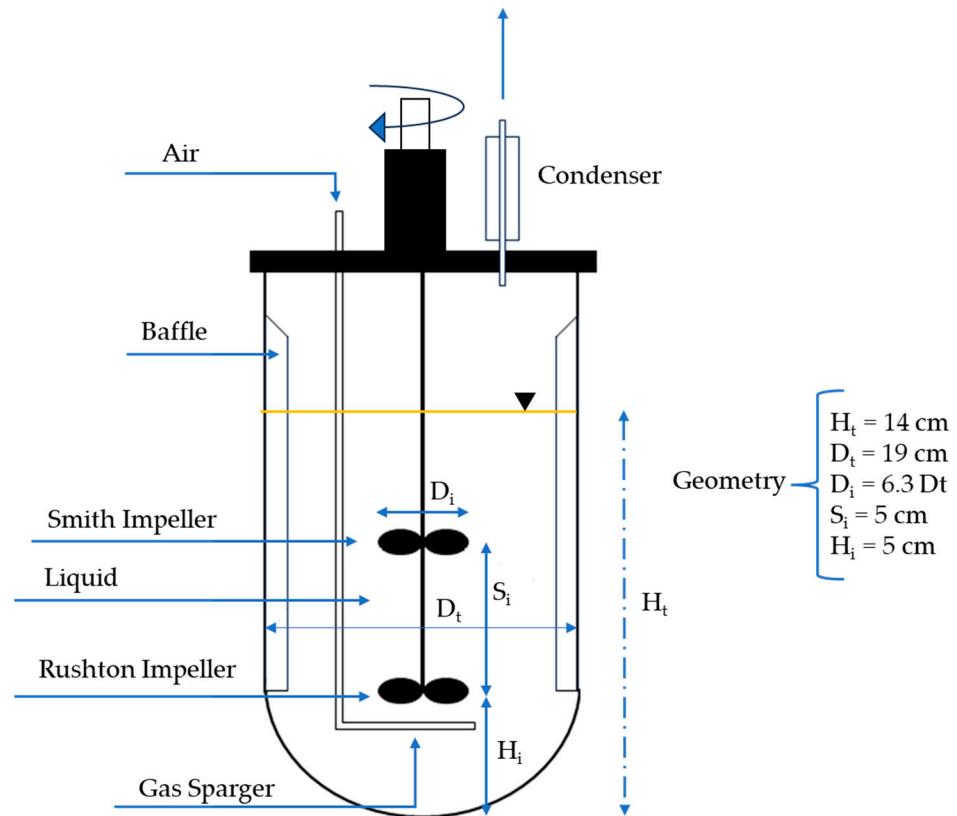


Figure 1. Dimensional scheme of the bioreactor.

Oxygen response curves were obtained by sparging nitrogen until the dissolved oxygen concentration fell to zero, then, continue with aeration at different operating conditions of aeration and agitation, to monitor the saturation oxygen concentration ( $C_L^*$ ) and oxygen concentration in the liquid ( $C_L$ ) as a function of time. The following Equation (1) is used to determine the  $k_La$  value.

$$\frac{dC_L}{dt} = N_{O_2} = k_{La} \times (C_L^* - C_L) \tag{1}$$

The equation can be integrated and result in Equation (2):

$$\ln \frac{(C_L^* - C_L)}{C_L^*} = k_{La} \times t \tag{2}$$

The graphic  $\ln(1 - C_L/C_L^*)$  versus time is a linear curve whose angular coefficient is the  $k_La$  value.

### 2.3. Influence of Silica Particles in the $k_La$

The influence of the particles in the coefficient of volumetric oxygen transfer was studied by varying the operating conditions of the system such as agitation speed (50–200 rpm), aeration rate (0.5–6.0 L min<sup>-1</sup>, corresponding to 0.17–2.0 vvm, respectively), particle size (approximate sizes: 10, 75, 150, and 350 μm), and the concentration of particles (0.05 to 5.0%, mgL<sup>-1</sup>).

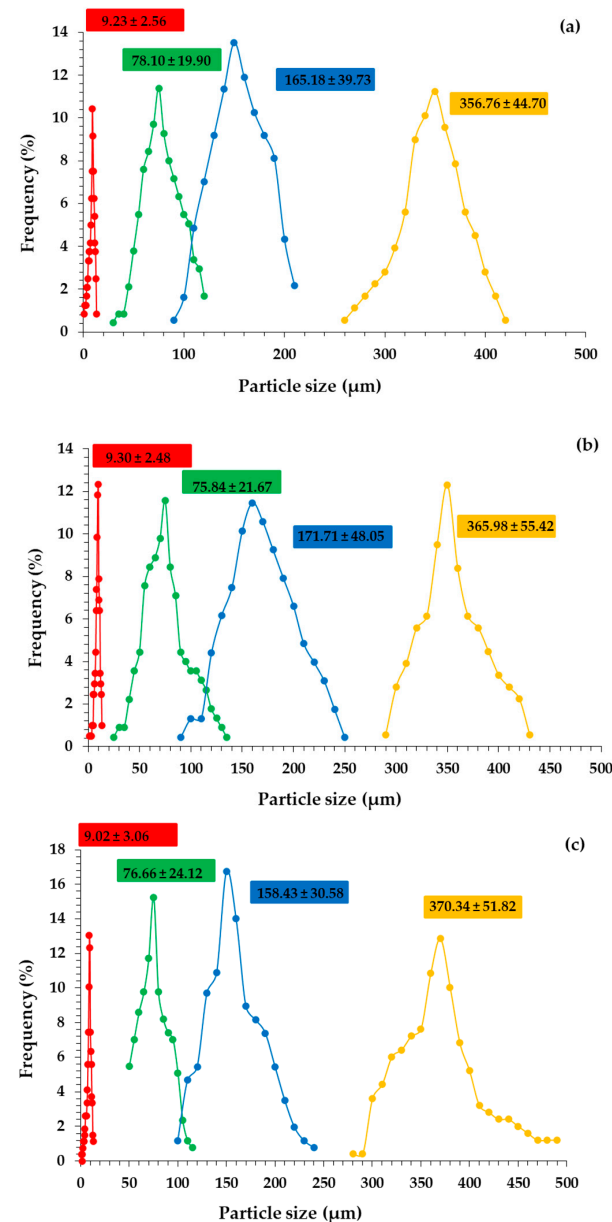
### 2.4. Statistical Analysis

The experimental data for studies on the influence of agitation speed, aeration rate, and the size and concentration of silica microparticles were compared using a Tukey test. The significance was established by ANOVA. Differences of  $p \geq 0.05$  were considered statistically significant.

### 3. Results and Discussion

#### 3.1. Production, Treatment, and Characterization of Silica Particles

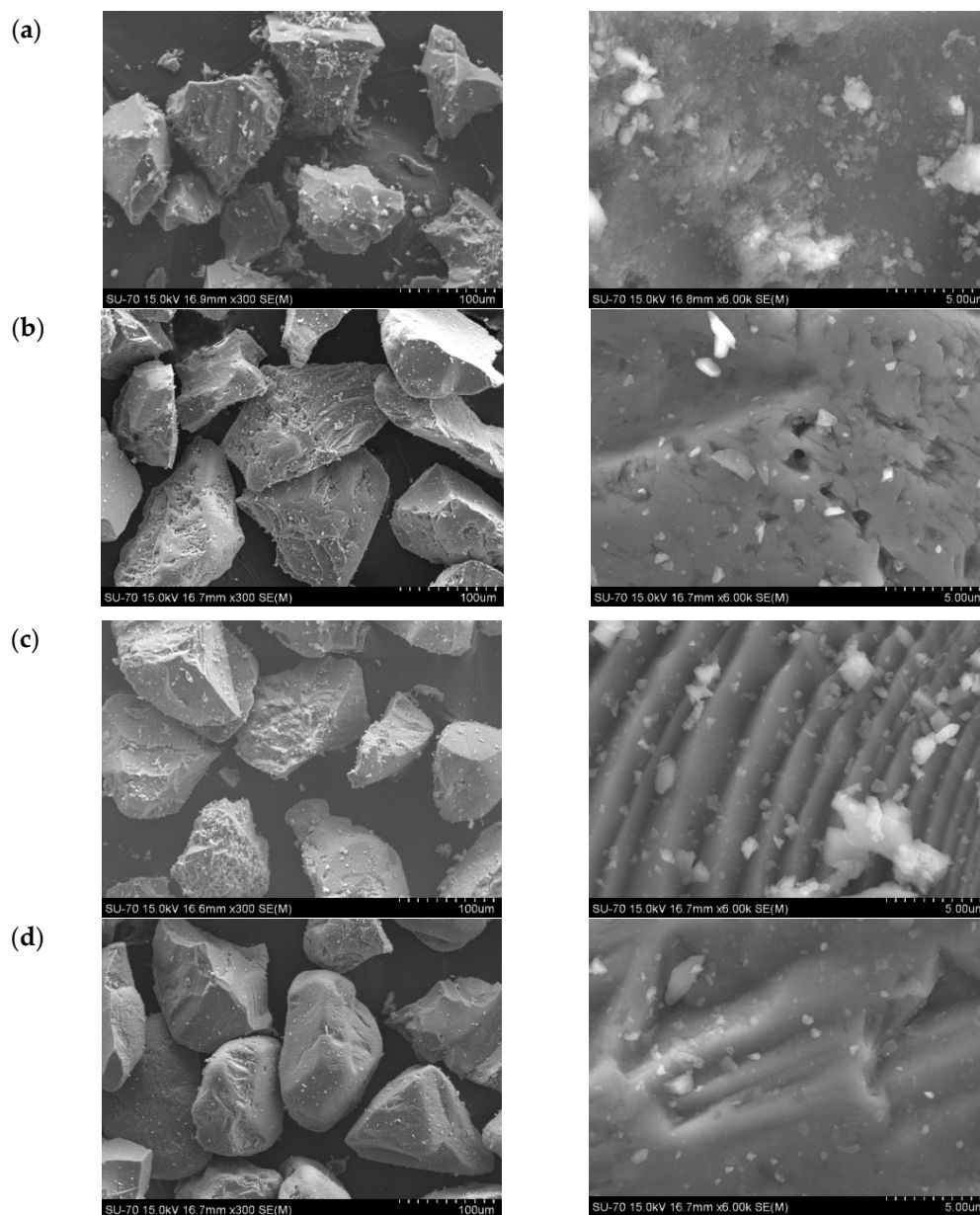
The silica sol-gel, commercial sand, and beach sand post-treatment with acid–base bath present different sizes; therefore, the samples were macerated and homogenized, reaching average sizes of 9.2, 76.9, 165.1, and 364.4  $\mu\text{m}$  in a Gaussian distribution of size, as shown in Figure 2.



**Figure 2.** Frequency of particle size distribution for silica sol-gel (a), commercial sand (b), and post-treatment beach sand (c).

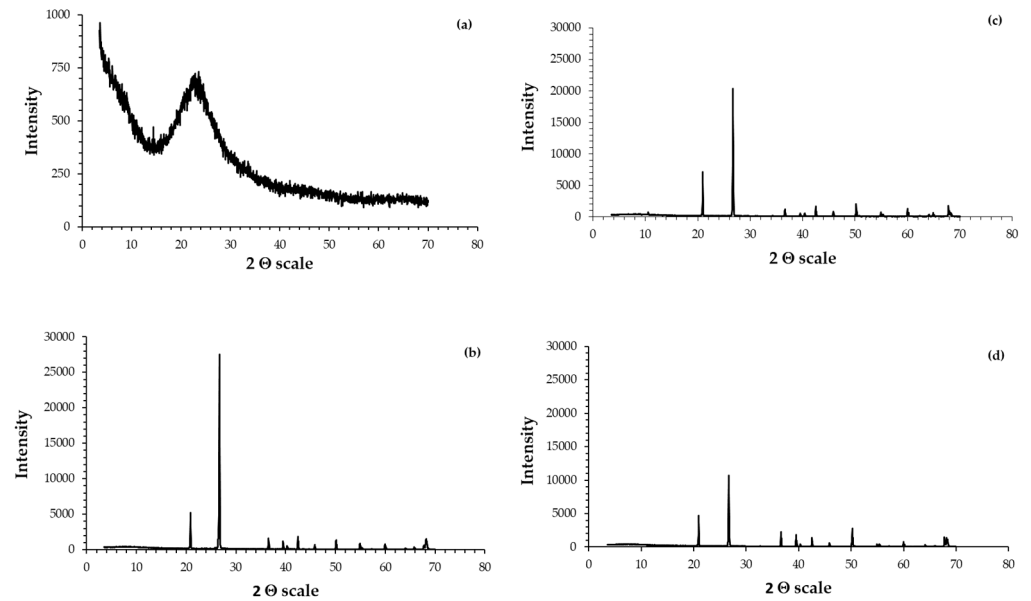
The iconographic analysis showed similarities among the silica microparticles (Supporting Information Figure S1). The Scanning Electronic Microscopy (SEM) image reveals the morphology of silica microparticles, which appear as irregular grains with different degrees of roughness (Figure 3). The silica sol-gel microparticles present a smooth surface, like the silicon dioxide. On the other hand, the beach sand pre- and post-treatment has a rough surface. The difference between beach sand and silica sol-gel can occur due to the calcination process, which is subject to silicon dioxide. The silanol groups are condensed to the surface from 150  $^{\circ}\text{C}$ , transforming the silanol groups into siloxanes, thus increas-

ing the hydrophobicity of the particles [26,27]. According to Zhao et al. [28], the silica films are transparent and continuous with smooth surfaces, as observed in this work for silica microparticles.



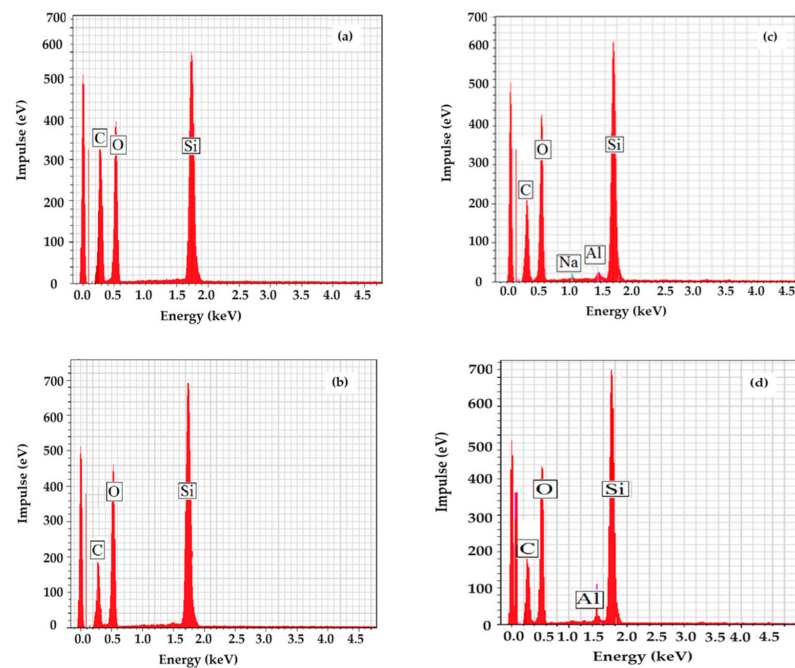
**Figure 3.** Scanning electronic microphotographs of silica microparticles. (a) Silica sol-gel, (b) commercial sand, (c) beach sand pre-treatment, and (d) beach sand post-treatment.

Figure 4 depicts the XRD intensity curves of silica microparticles, in which silica sol-gel presents amorphous characteristics due to the diffused and flat diffraction peaks over the angular range  $2\theta = 15\text{--}35^\circ$  [29,30]. In the other silicas, the peak intensity strongly indicates a crystalline nature [31] and appears at  $2\theta = 26^\circ$ . According to Yu et al. [32], silica sol-gel presents amorphous characteristics and is only crystalline. The sol-gel silica presented here was not calcined as the sands had suffered pressure and temperature changes over thousands of years. Silica sol-gel, commercial sand, and beach sand (post-treatment) mainly comprise silicon oxide. Moreover, the beach sand treatment using an acid–base concentrated bath provided the elimination of compounds bonded to silica, such as calcite, halite, fluorite, sodalite, and cordierite, becoming the post-treatment beach sand with a composition like silica sol-gel and commercial sand (Supporting Information Table S1).



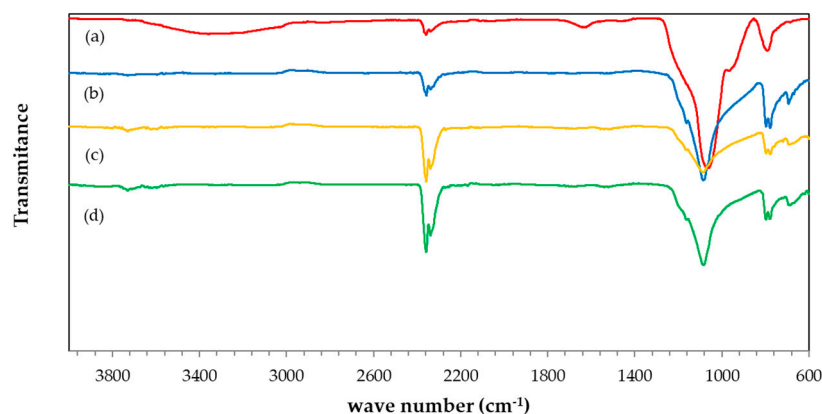
**Figure 4.** XRD patterns of (a) silica sol-gel, (b) commercial sand, (c) pre-treatment beach sand, and (d) post-treatment beach sand.

Corroborating data from X-rays, the assay of silica microparticles as per the EDS method identified that silica sol-gel, commercial sand, and beach sand post-treatment presented the same atomic composition (carbon, oxygen, and silicon), as shown in Figure 5. The samples provided a high signal regarding silica and oxygen (due to silicon dioxide). The presence of carbon was also observed. The pre-treatment beach sand contained signs of sodium due to sea salinity and aluminum due to cordierite observed in the XRD results. According to Badapalli et al. (2022) [33], silica, oxygen, and aluminum are common elements present in the sand. After the acid–base washing treatment of beach sand, the signal of the presence of sodium disappears, probably caused by the leaching of this element and the amplification of the Al signal.



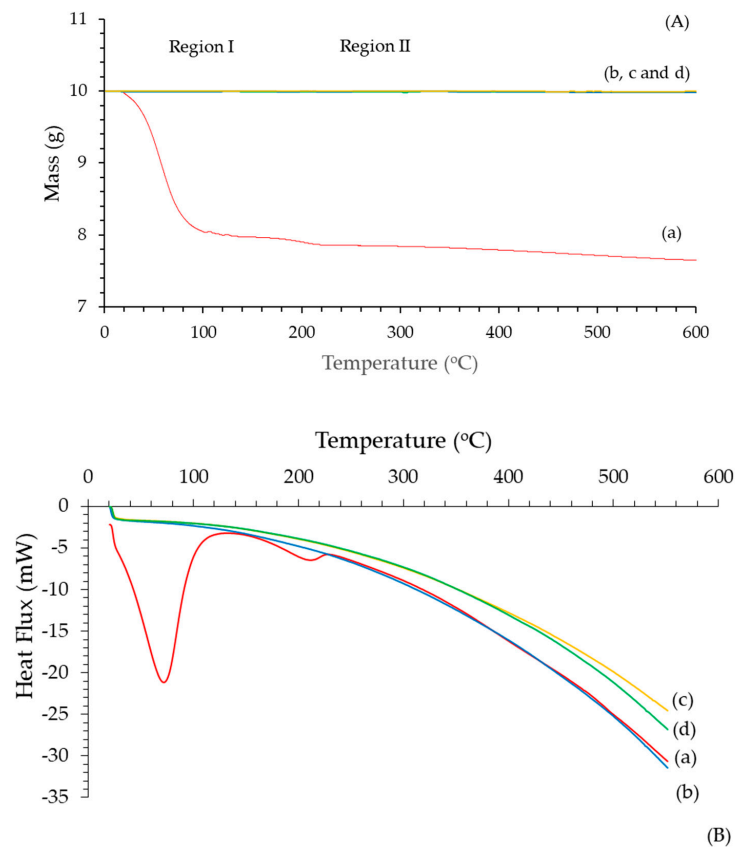
**Figure 5.** EDS spectrum, taken for the complete area, of the different microsilica materials: silica sol-gel (a), commercial sand (b), pre-treatment beach sand (c), and post-treatment beach sand (d).

Fourier-Transformed Infrared (FTIR) for silica is characterized by three main adsorption bands assigned to different vibration models. Figure 6 illustrates the FTIR spectra of silica microparticles used in this work. All peaks appear in the same position independent of the kind of silica microparticle. The spectra do not present the bands for the lowest frequency model (approximately  $460\text{ cm}^{-1}$ ), assigned to transverse optical ( $\text{TO}_1$ ) rocking motions perpendicular to the Si-O-Si plane of the oxygen bridging two adjacent Si atoms. The weak peaks of  $793\text{ cm}^{-1}$  are due to the asymmetric stretching vibration of the Si-OH (transverse optical— $\text{TO}_2$  model). The peaks between  $1087\text{--}1091\text{ cm}^{-1}$  are related to the transverse optical ( $\text{TO}_3$ ) model, which involves the motion back and forth of the oxygen atom along a line parallel to the Si-Si axis. The motion results in the opposite distortion of two neighboring Si-O bonds and is indicated as an asymmetric stretching vibration of Si-O [34]. According to Beganskiene et al. [35], peaks between  $800$  and  $1200\text{ cm}^{-1}$  correspond to the superimposition of several  $\text{SiO}_2$  peaks, Si-OH bonding, and eventual peaks due to residual organic groups. The peaks at  $2300\text{ cm}^{-1}$  correspond to the chemical bonds with the hydrogen  $\text{SiH}_x$  surface [36]. Finally, the absorption band around  $3100\text{--}3600\text{ cm}^{-1}$  represents the overlapping of the O-H stretching bands of hydrogen-bonded water molecules ( $\text{H-O-H}\cdots\text{H}$ ) and SiO-H stretching of surface silanols hydrogen-bonded to molecular water ( $\text{Si-O-H}\cdots\text{H}_2\text{O}$ ) [37].



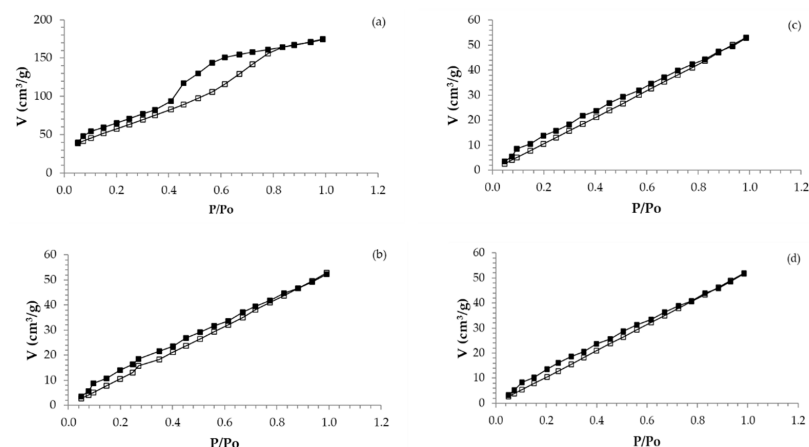
**Figure 6.** FTIR spectra of different microsilica materials: silica sol-gel (a), commercial sand (b), pre-treatment beach sand (c), and post-treatment beach sand (d).

Figure 7 depicts the TG analysis and DSC thermograms for different silica samples. Thermogravimetric Analysis (TGA) is based on the weight change of a sample when submitted to a heat or cool process in a controlled atmosphere and, therefore, is widely used to characterize a material [38]. The weight loss curves were divided into two regions to simplify the TG analysis (Figure 7A). Commercial sand, pre-treatment beach sand, and post-treatment beach sand had practically constant mass, with minimal weight losses of 0.17, 0.19, and 0.51%, denoting that there was no adsorbed water or dehydroxylation of the silicon oxide or silicon hydroxide. On the other hand, sol-gel silica showed a total mass loss of 24.5%. In Region I ( $0\text{--}200\text{ }^\circ\text{C}$ ), the weight loss corresponding to 21% was attributed to the elimination of residual reactants from the silica sol-gel preparation (e.g., silanol groups of tetraethyl orthosilicate—TEOS) and adsorbed water molecules [24]. Afterward ( $200\text{--}600\text{ }^\circ\text{C}$ —Region II), the loss of weight (3.5%) was due to the removal of water through dehydroxylation and the loss of organic constituents [39]. Figure 7B depicts the DSC thermogram for silica samples used in this work. Commercial sand, pre-treatment beach sand, and post-treatment beach sand did not present a significant heat flow. The silica sol-gel had two endothermic peaks at  $73\text{ }^\circ\text{C}$ , probably associated with ethanol evaporation [40], and another one at  $210\text{ }^\circ\text{C}$ , corresponding to a loss of bound water, trapped water into the pores, and/or the condensation of free or blocked OH groups, as also observed by Klingshirn et al. [41].



**Figure 7.** Thermogravimetric curves (A) and DSC (B) of different microsilia materials: silica sol-gel (a), commercial sand (b), pre-treatment beach sand (c), and post-treatment beach sand (d).

The nitrogen adsorption/desorption isotherms of the silica microparticles are shown in Figure 8. The isotherm by silica sol-gel is classified as type IV by IUPAC according to Sing et al. [42]. The hysteresis loop (Type H2) is associated with capillary condensation in mesopores; this hysteresis is attributed to a difference in mechanism between condensation and evaporation processes occurring in pores with narrow necks and wide bodies (ink bottle pores). For other silica microparticles, the isotherms are characterized as non-porous or macroporous (isotherms type II), and the loop is characterized by the hysteresis type H3 loop, which is observed with aggregates of plate-like particles giving rise to slit-shaped pores.



**Figure 8.** Gas adsorption/desorption isotherm obtained for silica microparticle. Silica sol-gel (a), commercial sand (b), pre-treatment beach sand (c), and post-treatment beach sand (d). □—adsorption and ■—desorption.

Table 1 shows the results of specific surface area (BET methods) and mean pore diameter and pore volume measurements for silica microparticles. The values for silica obtained via the sol-gel technique are noteworthy and agree with published data for similar systems [39,43,44]. However, the values of the surface area, pore diameter, and pore volume for the silica were higher than those found for silicon dioxide and beach sand post and pre-treatment, which were similar. The silica sol-gel was differentiated from the others due to its particles being obtained using the tetraethyl orthosilicate (TEOS) as a reagent, making it a highly porous particle.

**Table 1.** Silica microparticles: surface characterization.

Microparticle	Surface Area (m <sup>2</sup> g <sup>-1</sup> )	Mean Pore Diameter (Å)	Pore Volume (cm <sup>3</sup> g <sup>-1</sup> )
Silica	223.73	17.33	0.213
Commercial sand	90.36	17.13	0.071
Pre-treatment beach sand	89.50	15.33	0.079
Post-treatment beach sand	89.71	17.14	0.070

All results on the silica microparticle characteristics indicated that the commercial sand and beach sand (pre- and post-treatment) were similar; however, we decided to distinguish the silica produced via the sol-gel technique.

### 3.2. Effect of Agitation and Aeration on the Oxygen Mass Transference ( $k_L a$ )

Environmental conditions such as the temperature, pH, and composition of the culture medium, and operational conditions, such as agitation and aeration, are fundamental in conducting fermentative processes [45,46]. Operating conditions are linked to the bioreactor design, and the optimal conditions for performing the process depend, in the first instance, on the morphology of the microorganism used as a biological agent. Focusing on operational conditions, several authors report ranges of agitation for the fermentation process when bacteria [47,48] and yeast [49,50] are used or when filamentous fungi are used [51,52]. According to Cui et al. [23], the size and structure of fungal pellets (smooth or fluffy) are influenced by agitation, which can cause cell autolysis. Therefore, this work studied the effect of low agitation rates (50 and 200 rpm), intending to cover different microbial morphologies. Figure 9 (Table S2 of Supporting Information) illustrates the effect of agitation on the  $k_L a$  at a constant aeration of 1.5 L min<sup>-1</sup> (0.5 vvm) and 25 °C without silica microparticles. Moreover, limiting agitation is important to prevent the shearing of the biomass and thus enable the addition of silica microparticles.

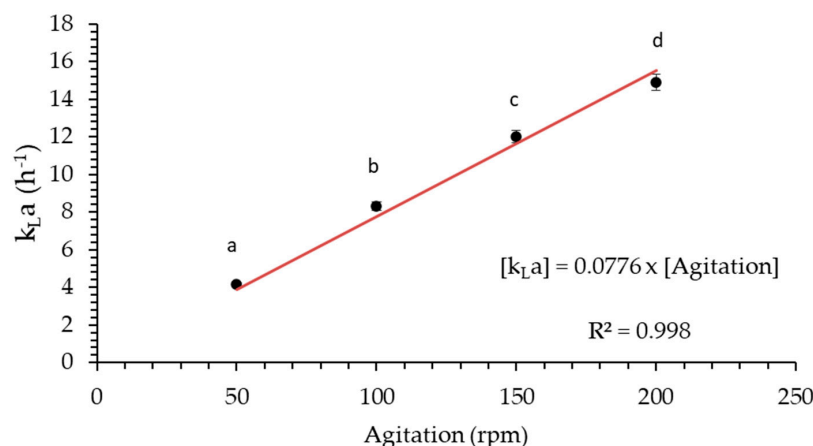


**Figure 9.** Influence of agitation on the oxygen mass transfer ( $k_L a$ ) using an aeration of 1.5 L min<sup>-1</sup> at 25 °C. Means followed by the same letter do not differ statistically as per Tukey test ( $p > 0.05$ ).

The  $k_L a$  increased from  $4.5 \text{ h}^{-1}$  (50 rpm) to  $14.91 \text{ h}^{-1}$  (200 rpm), probably due to the reduction in the air bubble size, increasing the bubble's surface area and consequently improving the  $k_L a$ . Using the Tukey method, we observed that the values had statistically significant difference ( $p \geq 0.05$ ). The correlation of  $k_L a$  versus agitation was linear ( $R^2 = 0.998$ ), which agreed with the results reported by the literature [53,54]. Moreover, Santos-Moreau et al. [55] reported higher turbulent energy dissipation with the rise of agitation, which increases the nominal  $k_L a$  value and areas with a high  $k_L a$  profile in the bioreactor. This increase in  $k_L a$  with agitation is also due to the relation to power per volume in the liquid phase and the gas hold-up in the fermenter [56].

The following experiments were conducted with an intermediate agitation speed of 100 rpm and a range of aeration from  $0.50 \text{ L min}^{-1}$  (0.17 vvm) to  $6.0 \text{ L min}^{-1}$  (2 vvm), as shown in Figure 10 (Table S3 of Supporting Information).

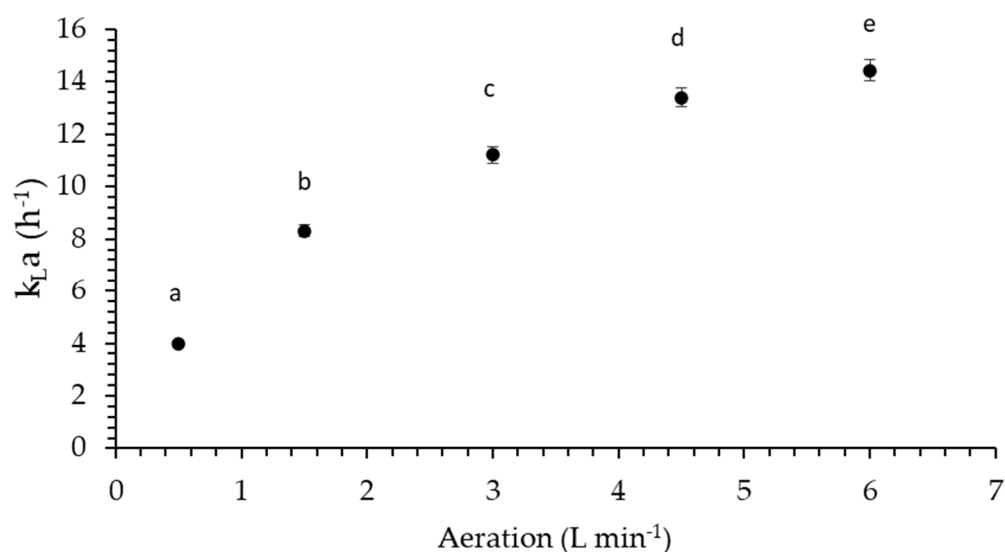


**Figure 10.** Influence of aeration on the oxygen mass transfer ( $k_L a$ ) using an agitation of 100 rpm at  $25 \text{ }^\circ\text{C}$ . Means followed by the same letter do not differ statistically as per Tukey test ( $p > 0.05$ ).

The results indicate an increase in  $k_L a$  from  $3.96$  to  $14.44 \text{ h}^{-1}$ , with a change in the slope of the tangent, which points to a steady state after aeration of  $6.0 \text{ L min}^{-1}$  as also observed by Özbek and Gayic [53]. However, the values are statistically different from each other ( $p \geq 0.05$ ). The data reported by Satitrueng and Sootitawat [56] present an inflection of the  $k_L a$  versus aeration graph at 1 vvm ( $3.0 \text{ L min}^{-1}$ ), leading to the aforementioned steady state. The volumetric mass transfer coefficient is formed by two terms: the first one is the mass transfer coefficient ( $k_L$ ), and the other one is the transfer air ( $a$ ). Both are affected by aeration [57] since it combines the effect of higher interfacial area per unit of gas volume of airflow that generates fine bubbles diffused in the bioreactor [58].

### 3.3. Effect of Silica Particles on the Oxygen Mass Transference ( $k_L a$ )

After choosing operating conditions (100 rpm of agitation and  $3.0 \text{ L min}^{-1}$  of aeration), the study was carried out, evaluating the effects of particle sizes—approximately 10, 75, 150, and  $350 \text{ }\mu\text{m}$  (Figure 11 and Table S4 of Supporting Information)—and particle concentrations (between  $0.05$  and  $5.00 \text{ g L}^{-1}$ ) (Figure 12 and Table S5 of Supporting Information). The silica microparticles reach the air bubble surface through the collision phenomenon; however, they neither adhere nor fix themselves to the surface due to their hydrophilic characteristics. Afterward, they enter the boundary layer, increasing the shear stress, and migrate to the bulk liquid [59]. In all systems studied, the addition of particles improves the  $k_L a$ . According to Zhang et al. [21], this result is due to the effect of particles, which are drawn into the interfacial region, deforming and reducing the boundary layer and

consequently decreasing the resistance of the boundary layer in the transfer of oxygen to the bulk liquid, thus increasing the value of  $k_L a$ .

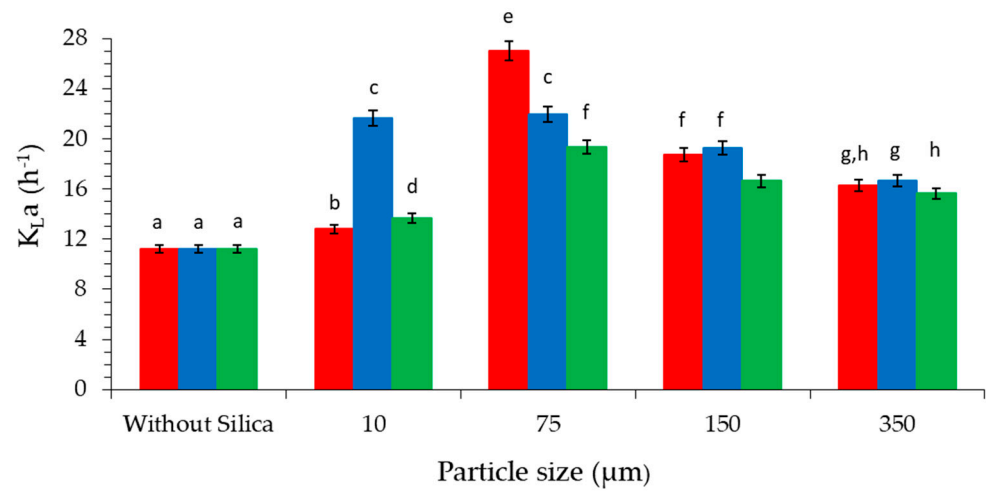


**Figure 11.** Effect of particle size ( $1 g L^{-1}$ ) on the oxygen mass transfer ( $k_L a$ ) using an agitation of  $100 rpm$  aeration of  $3.0 L min^{-1}$  at  $25^\circ C$ . ■—silica sol-gel, ■—commercial sand, and ■—beach sand (treated). Means followed by the same letter do not differ statistically as per Tukey test ( $p > 0.05$ ).

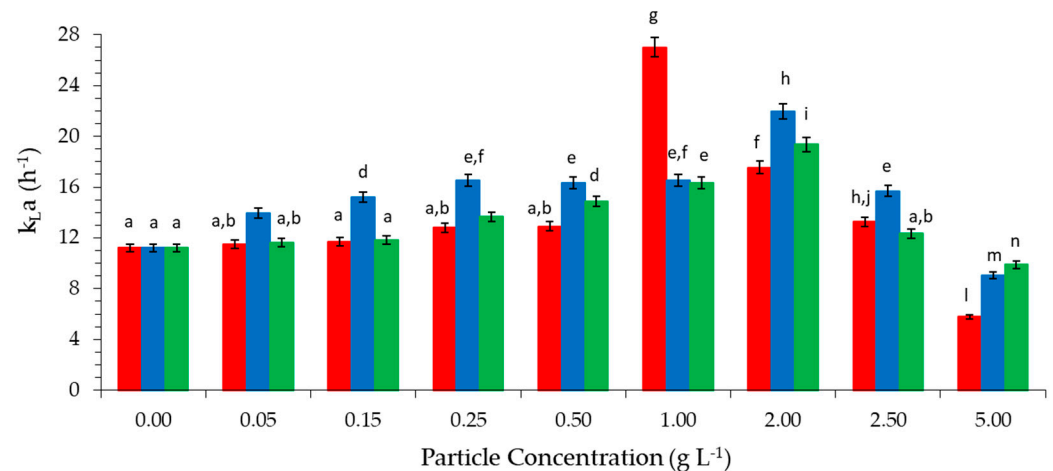


**Figure 12.** Effect of particle concentration with  $75 \mu m$  on the oxygen mass transfer ( $k_L a$ ) using an agitation of  $100 rpm$  aeration of  $3.0 L min^{-1}$  at  $25^\circ C$ . ■—silica sol-gel, ■—commercial sand, and ■—beach sand (treated). Means followed by the same letter do not differ statistically as per Tukey test ( $p > 0.05$ ).

Figure 11 clearly depicts the addition of silica particles at a concentration of  $1 g L^{-1}$  with a limit point occurring at  $75 \mu m$ , at which the  $k_L a$  reached maximum values of  $19.35$ ,  $21.95$ , and  $27.02 h^{-1}$  corresponding to increases of  $72.6$ ,  $95.81$ , and  $141.0\%$  for treated beach sand, commercial sand, and silica sol-gel, respectively. In this condition, the  $k_L a$  values were statistically different from each other ( $p \geq 0.05$ ) although the  $k_L a$  values for commercial sand at  $10$  and  $75$  were statistically similar. Small particles have a higher surface area, consequently allowing for a higher  $k_L a$  value [60]. However, the  $10 \mu m$  silica particles could not increase the  $k_L a$ , probably due to other factors such as the weak decreasing action of the boundary layer. On the other hand, Ozbek and Gayik [52] reported that bulky biomass particles at a low loading percentage increase the  $k_L a$  in a bioreactor using water as the fluid.

The effect of silica microparticle concentration on  $k_L a$  can be seen in Figure 12. The enrichment of the  $k_L a$  value with an increasing particle concentration occurs under different

limiting conditions. For silica sol-gel microparticles, the effect is observed up to  $1.00 \text{ g L}^{-1}$  ( $27.02 \text{ h}^{-1}$ ) while commercial sand and post-treatment beach sand reach a maximum of  $2.0 \text{ g L}^{-1}$  ( $21.95$  and  $19.35 \text{ h}^{-1}$ ). These optimal values of  $k_L a$  are statistically different from each other ( $p \geq 0.05$ ) according to the comparison of means using the Tukey method. The differences can be attributed to the larger surface area and pore volume for silica sol-gel in Table 1. This microparticle oxide transports oxygen more efficiently from the gas phase to the bulk phase and, therefore, has a higher  $k_L a$  value. Olle et al. [60] reported that small concentrations of particles increase the  $k_L a$ . However, these concentrations reach a threshold value and decrease again. Increasing the particle concentration above the threshold value increases the apparent viscosity of the medium, dampening bubbles breaking, allowing them to coalesce, increasing the interfacial area, and reducing the  $k_L a$  value. Low concentration increases the hold-up in bubble columns [20].

#### 4. Conclusions

The transfer of oxygen in mixing reactors is a point of interest in conducting aerobic fermentative processes because it interferes with the growth of the biological agent, which promotes the production of the target biomolecule. In this work, we chose to use small agitations to apply the conditions of fermentative processes using filamentous fungi. Operational parameters such as agitation and aeration increase the mass transfer coefficient in the bioreactor and mixture. However, adding silica microparticles, the best size of approximately  $75 \mu\text{m}$  can still improve these values. The best concentrations of silica microparticles depend on the type used, being  $1.0 \text{ g L}^{-1}$  ( $k_L a = 27.02 \text{ h}^{-1}$ ) for silica sol-gel and  $2.0 \text{ g L}^{-1}$  for sand commercial and treated beach sand ( $k_L a = 21.95$  and  $19.35 \text{ h}^{-1}$ , respectively). These differences are based on the characteristics of the particles.

**Supplementary Materials:** The following supporting information can be downloaded at: <https://www.mdpi.com/article/10.3390/fermentation10050255/s1>, Figure S1. Microscopy image of sol-gel silica (1), commercial sand (2), and treated beach sand (3): (A)  $350 \mu\text{m}$ , (B)  $150 \mu\text{m}$ , (C)  $75 \mu\text{m}$ , (D)  $10 \mu\text{m}$ ; Table S1. X-ray diffraction analysis of silica microparticles; Table S2. Influence of agitation on the oxygen mass transfer ( $k_L a$ ) using an aeration of  $1.5 \text{ L min}^{-1}$  at  $25 \text{ }^\circ\text{C}$ ; Table S3. Influence of agitation on the oxygen mass transfer ( $k_L a$ ) using an aeration of  $1.5 \text{ L min}^{-1}$  at  $25 \text{ }^\circ\text{C}$ ; Table S4. Effect of particle size ( $1 \text{ g L}^{-1}$ ) on the oxygen mass transfer ( $k_L a$ ) using an agitation of  $100 \text{ rpm}$  aeration of  $3.0 \text{ L min}^{-1}$  and at  $25 \text{ }^\circ\text{C}$ ; Table S5. Effect of particle concentration with  $75 \mu\text{m}$  on the oxygen mass transfer ( $k_L a$ ) using an agitation of  $100 \text{ rpm}$  aeration of  $3.0 \text{ L min}^{-1}$  and at  $25 \text{ }^\circ\text{C}$ .

**Author Contributions:** Conceptualization, E.B.C.; methodology, M.M.P. and I.L.O.M.; software, F.M.M.C.; validation, M.M.P.; formal analysis, I.L.O.M.; investigation, A.C.M.d.S.; resources, data curation, Á.S.L.; writing—original draft preparation, E.B.C. and A.C.M.d.S.; writing—review and editing, Á.S.L.; visualization, M.M.P. and F.M.M.C.; supervision, A.C.M.d.S. and E.B.C.; project administration, Á.S.L.; funding acquisition, Á.S.L. All authors have read and agreed to the published version of the manuscript.

**Funding:** This research was funded by CNPq, grant number 302988/2019-0. Matheus M. Pereira acknowledges the financial support of FCT, Portugal, within the projects DOI: 10.54499/UIDB/00102/2020 (Base funding) and DOI: 10.54499/UIDP/00102/2020 (Programmatic funding).

**Data Availability Statement:** Data are contained within the article.

**Acknowledgments:** The authors express their gratitude to administrative and technical support of ITP.

**Conflicts of Interest:** The authors declare no conflicts of interest.

#### References

1. Borisov, V.B.; Verkhovsky, M.I. Oxygen as acceptor. *EcoSal Plus* **2022**, *6*, 10128. [CrossRef]
2. Suresh, S.; Srivastava, V.C.; Mishra, I.M. Techniques for oxygen transfer measurement in bioreactors: A review. *J. Chem. Technol. Biotechnol.* **2009**, *84*, 1091–1103. [CrossRef]

3. Wang, Z.J.; Wang, H.Y.; Li, Y.L.; Chu, J.; Huang, M.Z.; Zhuang, Y.P.; Zhang, S.L. Improved vitamin B12 production by step-wise reduction of oxygen uptake rate under dissolved oxygen limiting level during fermentation process. *Bioresour. Technol.* **2020**, *101*, 2845–2852. [[CrossRef](#)] [[PubMed](#)]
4. Gamboa-Suasnavart, R.A.; Valdez-Cruz, N.A.; Gaytan-Ortega, G.; Reynoso-Cerecedal, G.I.; Cabrera-Santos, D.; López-Griegol, L.; Klöckner, B.J.; Trujillo-Roldán, M.A. The metabolic switch can be activated in a recombinant strain of *Streptomyces lividans* by a low oxygen transfer rate in shake fasks. *Microb. Cell Factories.* **2018**, *17*, 189. [[CrossRef](#)] [[PubMed](#)]
5. Garcia-Ochoa, F.; Gomez, E.; Santos, V.E.; Merchuk, J.C. Oxygen uptake rate in microbial processes: An overview. *Biochem. Eng. J.* **2010**, *49*, 289–307. [[CrossRef](#)]
6. Ju, L.K.; Ho, C.S.; Baddour, R.F. Simultaneous measurements of oxygen diffusion coefficients and solubilities in fermentation media with polarographic oxygen electrodes. *Biotechnol. Bioeng.* **1988**, *31*, 995–1005. [[CrossRef](#)]
7. Tromans, D. Temperature and pressure dependent solubility of oxygen in water: A thermodynamic analysis. *Hydrometallurgy* **1998**, *48*, 327–342. [[CrossRef](#)]
8. Ntwampe, S.K.O.; Williams, C.C.; Sheldon, M.S. Water immiscible dissolved oxygen carries in combination with pluronic F 68 in bioreactors. *Afr. J. Biotechnol.* **2010**, *9*, 1106–1114. [[CrossRef](#)]
9. Vieira, E.S.; Fontes, T.K.O.; Pereira, M.M.; Alexandre, H.V.; Silva, D.P.; Soares, C.M.F.; Lima, A.S. New strategy to apply perfluorodecalin as an oxygen carrier in lipase production: Minimisation and reuse. *Bioprocess Biosyst. Eng.* **2015**, *38*, 721–728. [[CrossRef](#)]
10. Amaral, P.F.F.; Rocha-Leão, M.H.M.; Marrucho, I.M.; Coutinho, J.A.P.; Coelho, M.A.Z. Improving lipase production using a perfluorocarbon as oxygen carrier. *J. Chem. Technol. Biotechnol.* **2006**, *81*, 1368–1374. [[CrossRef](#)]
11. Littlejohns, J.V.; Daugulis, A.J. Oxygen transfer in a gas–liquid system containing solids of varying oxygen affinity. *Chem. Eng. J.* **2007**, *129*, 67–74. [[CrossRef](#)]
12. Olle, B.; Wang, D.I.C. Novel and new concept to increase oxygen transfer in bioreactors. *Chem. Eng. Trans.* **2008**, *14*, 1–12.
13. Shet, A.S.; Shetty, K.V. TiO<sub>2</sub> nanofluid for oxygen mass transfer intensification in pulsed plate column. *Chem. Eng. Commun.* **2021**, *208*, 1653–1675. [[CrossRef](#)]
14. Krishnamurthy, S.; Bhattacharya, P.; Phelan, P.E.; Prasher, R.S. Enhanced mass transport in nanofluids. *Nano Lett.* **2006**, *6*, 419–423. [[CrossRef](#)] [[PubMed](#)]
15. Martínez, D.T.; Torres, R.M.; Rojas, M.G.; Vázquez, L.A.; Micheletti, M.; Lye, G.J.; Ochoa, S.H. Hydrodynamic and oxygen mass transfer studies in a three-phase (air–water–ionic liquid) stirred tank bioreactor. *Biochem. Eng. J.* **2009**, *45*, 209–217. [[CrossRef](#)]
16. Labbeiki, G.; Attar, H.; Heydarinasab, A.; Sorkhabadi, S.; Rashidi, A. Enhanced oxygen transfer rate and bioprocess yield by using magnetite nanoparticles in fermentation media of erythromycin. *J. Pharm. Sci.* **2014**, *22*, 66. [[CrossRef](#)]
17. Fatollahi, P.; Ghasemi, M.; Yazdian, F.; Sadeghi, A. Ectoine production in bioreactor by *Halomonas elongate* DSM2581: Using MWCNT and Fe-nanoparticle. *Biotechnol. Progress.* **2021**, *37*, 23073. [[CrossRef](#)]
18. Esperança, M.N.; Cunha, F.M.; Cerri, M.O.; Zangirolami, T.C.; Farinas, C.S.; Badino, A.C. Gas hold-up and oxygen mass transfer in three pneumatic bioreactors operating with sugarcane bagasse suspensions. *Bioprocess Biosyst. Eng.* **2014**, *37*, 805–812. [[CrossRef](#)]
19. Ojima, S.; Sasaki, S.; Hayashi, K.; Tomiyama, A. Effects of particle diameter on bubble coalescence in a slurry bubble column. *J. Chem. Eng. Jpn.* **2015**, *48*, 181–189. [[CrossRef](#)]
20. Sasaki, S.; Uchida, K.; Hayashi, K.; Tomiyama, A. Effect of particle concentration and slurry height on gas holdup in a slurry bubble column. *J. Chem. Eng. Jpn.* **2016**, *49*, 824–830. [[CrossRef](#)]
21. Zhang, S.; Wang, D.; Fan, P.P.; Sun, L.P. Enhancement of gas-to-liquid oxygen transfer in the presence of fine solid particles for air-exposed multiphase system. *Chem. Eng. Res. Des.* **2015**, *100*, 434–443. [[CrossRef](#)]
22. Mokwatlo, S.C.; Brink, H.G.; Nicol, W. Effect of shear on morphology, viability and metabolic activity of succinic acid-producing *Actinobacillus succinogenes* biofilms. *Bioprocess and Biosyst. Eng.* **2020**, *43*, 1253–1263. [[CrossRef](#)] [[PubMed](#)]
23. Cui, Y.Q.; van der Lans, R.G.J.M.; Luyben, K.C.A.M. Effect of agitation intensities on fungal morphology of submerged fermentation. *Biotechnol. Bioeng.* **1997**, *55*, 715–726. [[CrossRef](#)]
24. Soares, C.M.F.; Santos, O.A.; Olivio, J.E.; Castro, H.F.; Moraes, F.F.; Zaniin, G.M. Influence of the alkyl-substituted silane precursor on sol-gel encapsulated lipase activity. *J. Mol. Catal. B* **2004**, *29*, 69–79. [[CrossRef](#)]
25. Soares, C.M.F.; Santos, O.A.; Castro, H.F.; Moraes, F.F.; Zanin, G.M. Studies on lipase immobilization in hydrophobic sol-gel matrix. *Appl. Biochem. Biotechnol.* **2004**, *113*, 307–319. [[CrossRef](#)]
26. Lin, J.; Chen, H.; Yao, L. Surface tailoring of SiO<sub>2</sub> nanoparticles by mechanochemical method based on simple milling. *Appl. Surf. Sci.* **2010**, *256*, 5978–5984. [[CrossRef](#)]
27. Iler, R.K. *The Chemistry of Silica*; John Wiley & Sons: New York, NY, USA, 1979.
28. Zhao, D.; Yang, P.; Melosh, N.; Feng, J.; Chmelka, B.F.; Stucky, G.D. Continuous mesoporous silica film with highly ordered large pore structures. *Adv. Mater.* **1998**, *10*, 1380–1385. [[CrossRef](#)]
29. Biswas, R.K.; Khan, P.; Mukherjee, S.; Mukhopahyay, A.K.; Ghosh, J.; Muraleedharan, K. Study of short range structure of amorphous Silica from PDF using Ag radiation in laboratory XRD system, RAMAN and NEXAFS. *J. Non-Cryst. Solids.* **2018**, *488*, 1–9. [[CrossRef](#)]
30. Popa, A.; Sasca, V.; Kiss, E.E.; Marinkovic-Neducin, R.; Bokorov, M.T.; Holclajtner-Antunovi, I. Studies in structural characterization of silica–heteropolyacids composites prepared by sol–gel method. *Mater. Chem. Phys.* **2010**, *119*, 465–470. [[CrossRef](#)]

31. Mechri, M.L.; Chihi, S.; Mahdadi, N.; Beddiaf, S. Study of heat effect on the composition of dunes sand of Ouargla (Algeria) using XRD and FTIR. *Silicon* **2017**, *9*, 933–941. [[CrossRef](#)]
32. Yu, L.Y.; Huang, Z.X.; Shi, M.X. Synthesis and characterization of silica by sol-gel method. *Adv. Mater. Res.* **2014**, *1030–1031*, 189–192. [[CrossRef](#)]
33. Badapalli, P.K.; Kottala, R.B.; Rajasekhar, M.; Ramachandra, M.; Krupavathi, C. Modeling of comparative studies on surface micro morphology of Aeolian, River Lake, and beach sand samples using SEM and EDS/EDAX. *Mater. Today Proc.* **2022**, *50*, 655–660. [[CrossRef](#)]
34. Innocenzi, P. Infrared spectroscopy of sol-gel derived silica-based films: A spectra-microstructure overview. *J. Non-Cryst. Solids.* **2003**, *316*, 309–319. [[CrossRef](#)]
35. Beganskienė, A.; Sirutkaitis, V.; Kurtinaitienė, M.; Juškėnas, R.; Kareiva, A. FTIR, TEM and NMR investigations of Stöber silica nanoparticles. *Mater. Sci.* **2004**, *10*, 287–290.
36. Vásquez-A., M.A.; Rodríguez, G.A.; García-Salgado, G.; Romero-Paredes, G.; Peña-Sierra, R. FTIR and photoluminescence studies of porous silicon layers oxidized in controlled water vapor conditions. *Rev. Mex. Fis.* **2007**, *53*, 431–435.
37. Al-Oweini, R.; El-Rassy, H. Synthesis and characterization by FTIR spectroscopy of silica aerogels prepared using several Si(OR)<sub>4</sub> and R'Si(OR')<sub>3</sub> precursors. *J. Mol. Struct.* **2009**, *919*, 140–145. [[CrossRef](#)]
38. Tiwari, M.; Sahu, S.K.; Rathod, T.; Bhangare, R.C.; Ajmal, P.Y.; Pulhani, V.; Kumar, A.V. Comprehensive review on sampling, characterization and distribution of microplastics in beach sand and sediments. *Trends Environ. Anal. Chem.* **2023**, *40*, e00221. [[CrossRef](#)]
39. Souza, R.L.; Faria, E.L.P.; Figueiredo, R.T.; Freitas, L.S.; Iglesias, M.; Mattedi, S.; Zanin, G.M.; Santos, O.A.A.; Coutinho, J.A.P.; Lima, A.S.; et al. Protic ionic liquid as additive on lipase immobilization using silica sol-gel. *Enzym. Microb. Technol.* **2013**, *52*, 141–150. [[CrossRef](#)] [[PubMed](#)]
40. Pinheiro, R.C.; Soares, C.M.F.; Santos, O.A.A.; Castro, H.F.; Moraes, F.F.; Zanin, G.M. Influence of gelation time on the morphological and physico-chemical properties of the sol-gel entrapped lipase. *J. Mol. Catal. B Enzym.* **2008**, *52–53*, 27–33. [[CrossRef](#)]
41. Klingshirn, M.A.; Spear, S.K.; Holbrey, J.D.; Rogers, R.D. Ionic liquids as solvent and solvent additives for the synthesis of sol-gel materials. *J. Mater. Chem.* **2005**, *15*, 5174–5180. [[CrossRef](#)]
42. Sing, K.S.W.; Everett, D.H.; Haul, R.A.W.; Moscou, L.; Pierotti, R.A.; Rouquerol, J.; Siemieniewska, T. Reporting physisorption data for gas/solid systems with special reference to the determination of surface area and porosity (recommendations 1984). *Pure Appl. Chem.* **1985**, *57*, 603–619. [[CrossRef](#)]
43. Sdiri, A.; Higashi, T.; Bouaziz, S.; Benziana, M. Synthesis and characterization of silica gel from siliceous sands of southern Tunisia. *Arab. J. Chem.* **2014**, *7*, 486–493. [[CrossRef](#)]
44. Hadinia, N.; Dovom, M.R.E.; Yavarmansh, M. The effect of fermentation conditions (temperature, salt concentration, and pH) with lactobacillus strains for producing short chain fatty acids. *LWT* **2022**, *165*, 113709. [[CrossRef](#)]
45. Degeest, B.; Mozzi, F.; De Vuyst, L. Effect of medium composition and temperature and pH changes on exopolysaccharide yields and stability during *Streptococcus thermophilus* LY03 fermentations. *Int. J. Food Microbiol.* **2002**, *79*, 161–174. [[CrossRef](#)] [[PubMed](#)]
46. Kuo, H.-C.; Kwong, H.K.; Chen, H.-Y.; Hsu, H.-Y.; Yu, S.-H.; Hsieh, C.-W.; Lin, H.-W.; Chu, Y.-L.; Cheng, K.-C. Enhanced antioxidant activity of *Chenopodium formosanum* Koidz. by lactic acid bacteria: Optimization of fermentation conditions. *PLoS ONE* **2021**, *16*, e0249250. [[CrossRef](#)] [[PubMed](#)]
47. Wang, T.; Lu, Y.; Yan, H.; Li, X.; Wang, X.; Shan, Y.; Yi, Y.; Liu, B.; Zhou, Y.; Lü, X. Fermentation optimization and kinetic model for high cell density culture of a probiotic microorganism: *Lactobacillus rhamnosus* LS-8. *Bioprocess Biosyst. Eng.* **2020**, *43*, 515–528. [[CrossRef](#)] [[PubMed](#)]
48. López-Trujillo, J.; Mellado-Bosque, M.; Ascacio-Valdés, J.A.; Prado-Barragán, L.A.; Hernández-Herrera, J.A.; Aguilera-Carbó, A.F. Temperature and pH Optimization for Protease Production Fermented by *Yarrowia lipolytica* from Agro-Industrial Waste. *Fermentation* **2023**, *9*, 819. [[CrossRef](#)]
49. Guo, Q.; Zaved, H.; Zhang, H.; Wang, X.; Yun, J.; Zhang, G.; Yang, M.; Sun, W.; Qi, X. Optimization of fermentation medium for a newly isolated yeast strain (*Zygosaccharomyces rouxii* JM-C46) and evaluation of factors affecting biosynthesis of D-arabitol. *LWT* **2019**, *99*, 319–327. [[CrossRef](#)]
50. Alahmad, H.; Yazji, S.; Azizieh, A. Optimization of protease production from *Rhizomucor miehei* Rm4 isolate under solid-state fermentation. *J. Genet. Eng. Biotechnol.* **2022**, *20*, 82. [[CrossRef](#)]
51. Aboyeji, O.O.; Oloke, J.K.; Arinkoola, A.O.; Oke, M.A.; Ishola, M.M. Optimization of media components and fermentation conditions for citric acid production from sweet potato peel starch hydrolysate by *Aspergillus niger*. *Sci. Afr.* **2020**, *10*, e00554. [[CrossRef](#)]
52. Özbek, B.; Gayic, S. The studies on the oxygen mass transfer coefficient in a bioreactor. *Process Biochem.* **2001**, *36*, 729–741. [[CrossRef](#)]
53. Bandaipheth, C.; Prasertsan, P. Effect of aeration and agitation rates and scale-up on oxygen transfer coefficient,  $k_L a$  in exopolysaccharide production from *Enterobacter cloacae* WD7 C. *Carbohydr. Polym.* **2006**, *66*, 216–228. [[CrossRef](#)]
54. Santos-Moreau, V.; Lopes, J.C.B.; Fonte, C.P. Estimation of  $k_L a$  values in bench-scale stirred tank reactors with self-inducing impeller by multiphase CFD simulations. *Chem. Eng. Technol.* **2019**, *42*, 1545–1554. [[CrossRef](#)]
55. Satitrueng, K.; Soottitawat, A. Influence of agitator speed and aeration rate on the oxygen mass transfer rate coefficient in the stirred tank bioreactor. *J. Funct. Mater. Chem. Eng.* **2019**, *1*, 83–88.

56. Chern, J.M.; Yu, C.F. Oxygen transfer modelling of diffused aeration systems. *Ind. Eng. Chem. Res.* **1997**, *36*, 5447–5453. [[CrossRef](#)]
57. McWhirter, J.R.; Hutter, J.C. Improved oxygen mass transfer modelling for diffused/subsurface aeration systems. *AIChE J.* **1989**, *35*, 1527–1534. [[CrossRef](#)]
58. Lakhdissi, E.M.; Soleimani, I.; Guy, C.; Chaouki, J. Simultaneous effect of particle size and solid concentration on the hydrodynamics of slurry bubble column reactors. *AIChE J.* **2020**, *66*, e16813. [[CrossRef](#)]
59. Ding, C.; Xu, C.; He, T.; Liu, X.; Zhu, Y.; Sun, L.; Ouyang, J.; Gu, X. Oxygen mass transfer enhancement by activated carbon particles in xylose fermentation media. *Bioprocess Biosyst. Eng.* **2023**, *46*, 15–23. [[CrossRef](#)]
60. Olle, B.; Bucak, S.; Holmes, T.C.; Bromberg, L.; Hatton, T.A.; Wang, D.I.C. Enhancement of oxygen mass transfer using functionalized magnetic nanoparticles. *Ind. Eng. Chem. Res.* **2006**, *45*, 4355–4363. [[CrossRef](#)]

**Disclaimer/Publisher’s Note:** The statements, opinions and data contained in all publications are solely those of the individual author(s) and contributor(s) and not of MDPI and/or the editor(s). MDPI and/or the editor(s) disclaim responsibility for any injury to people or property resulting from any ideas, methods, instructions or products referred to in the content.